saline solution containing hydrogen peroxide, particularly, when the applied stress exceeds the critical stress for martensite transformation. The probable cause of the fracture is localized corrosion associated with the preferential dissolution of nickel ions. This may be one reason for the fracture of Ni-Ti superelastic alloy *in vivo*.

References

1. Wayman CM. Some applications of shape-memory alloys. J Met 1980;32:129–137.
2. Shabalovskaya SA. On the nature of the biocompatibility and on medical applications of NiTi shape memory and superelastic alloys. Biomed Mater Eng 1996;6:267–289.
3. Duerig T, Pelton A, Stöckel D. An overview of nitinol medical applications. Mater Sci Eng A 1999;273–275:149–160.
4. Morgan NB. Medical shape memory alloy applications—The market and its products. Mater Sci Eng A 2004;378:16–23.
5. Miyazaki S, Otsuka K. Development of shape memory alloys. ISIJ Int 1989;29:353–377.
6. Rondelli G. Corrosion resistance tests on NiTi shape memory alloy. Biomaterials 1996;17:2003–2008.
7. Wever DJ, Veldhuizen AG, de Vries J, Busscher HJ, Uges DRA, van Horn JR. Electrochemical and surface characterization of a nickel-titanium alloy. Biomaterials 1998;19:761–769.
8. Rondelli G, Vicentini B. Localized corrosion behaviour in simulated human body fluids of commercial Ni-Ti orthodontic wires. Biomaterials 1999;20:785–792.
9. Huang HH, Chiu YH, Lee TH, Wu SC, Yang HW, Su KH, Hsu CC. Ion release from NiTi orthodontic wires in artificial saliva with various acidities. Biomaterials 2003;24:3585–3592.
10. Carroll WM, Kelly MJ. Corrosion behavior of nitinol wires in body fluid environments. J Biomed Mater Res A 2003;67:1123–1130.
11. Pound BG. Susceptibility of nitinol to localized corrosion. J Biomed Mater Res A 2006;77:185–191.
12. Heintz C, Riepe G, Birken L, Kaiser E, Chakfé N, Morlock M, Delling G, Imig H. Corroded nitinol wires in explanted aortic endografts: An important mechanism of failure? J Endovasc Ther 2001;8:248–253.
13. Duda SH, Pusich B, Richter G, Landwehr P, Oliva VL, Tielbeek A, Wiesinger B, Hak JB, Tielemans H, Ziemer G, Cristea E, Lansky A, Bérégi JP. Sirolimus-eluting stents for the treatment of obstructive superficial femoral artery disease. Circulation 2002;106:1505–1509.
14. Jacobs TS, Won J, Gravereaux EC, Faries PL, Morrissey N, Teodorescu VJ, Hollier LH, Marin ML. Mechanical failure of prosthetic human implants: A 10-year experience with aortic stent graft devices. J Vasc Surg 2003;37:16–26.
15. Knirsch W, Haas NA, Lewin MAG, Uhlemann F. Longitudinal stent fracture 11 months after implantation in the left pulmonary artery and successful management by a stent-in-stent maneuver. Catheter Cardiovasc Interv 2003;58:116–118.
16. Babalık E, Gülbaran M, Gürmen T, Öztürk S. Fracture of popliteal artery stents. Circ J 2003;67:643–645.
17. Scheinert D, Scheinert S, Sax J, Piorkowski C, Bräunlich S, Ulrich M, Biamino G, Schmidt A. Prevalence and clinical impact of stent fractures after femoropopliteal stenting. J Am Coll Cardiol 2005;45:312–315.
18. Tengvall P, Elwing H, Sjöqvist L, Lundström I, Bjursten LM. Interaction between hydrogen peroxide and titanium: A possible role in the biocompatibility of titanium. Biomaterials 1989;10:118–120.
19. Tengvall P, Lundström I, Sjöqvist L, Elwing H, Bjursten LM. Titanium-hydrogen peroxide interaction: Model studies of the influence of the inflammatory response on titanium implants. Biomaterials 1989;10:166–175.
20. Pan J, Thierry D, Leygraf C. Electrochemical and XPS studies of titanium for biomaterial applications with respect to the effect of hydrogen peroxide. J Biomed Mater Res 1994;28:113–122.
21. Shabalovskaya SA. Biological aspects of TiNi alloy surfaces. J Phys IV 1995;5:1199–1204.
22. Fonseca C, Barbosa MA. Corrosion behaviour of titanium in biofluids containing H_2O_2 studied by electrochemical impedance spectroscopy. Corros Sci 2001;43:547–559.
23. Bearinger JP, Orme CA, Gilbert JL. Effect of hydrogen peroxide on titanium surfaces: In situ imaging and step-polarization impedance spectroscopy of commercially pure titanium and titanium, 6-aluminum, 4-vanadium. J Biomed Mater Res A 2003;67:702–712.
24. Yokoyama K, Kaneko K, Moriyama K, Asaoka K, Sakai J, Nagumo M. Delayed fracture of Ni-Ti superelastic alloys in acidic and neutral fluoride solutions. J Biomed Mater Res A 2004;69:105–113.
25. Yokoyama K, Kaneko K, Yabuta E, Asaoka K, Sakai J. Fracture of nickel-titanium superelastic alloy in sodium hypochlorite solution. Mater Sci Eng A 2004;369:43–48.
26. Sugimoto K. A technical agreement for the determination of transformation temperature in shape memory alloys by means of DSC. Netsu Sokutei. 1986;13:110–111.
27. Thierry B, Tabrizian M, Savadogo O, Yahia L'H. Effect of sterilization processes on NiTi alloy: Surface characterization. J Biomed Mater Res 2000;49:88–98.
28. Montague A, Merritt K, Brown S, Payer J. Effects of Ca and H_2O_2 added to RPMI on the fretting corrosion of Ti6Al4V. J Biomed Mater Res 1996;32:519–526.
29. Mu Y, Kobayashi T, Sumita M, Yamamoto A, Hanawa T. Metal ion release from titanium with active oxygen species generated by rat macrophages *in vitro*. J Biomed Mater Res 2000;49:238–243.
30. Pan J, Thierry D, Leygraf C. Electrochemical impedance spectroscopy study of the passive oxide film on titanium for implant application. Electrochim Acta 1996;41:1143–1153.
31. Pan J, Thierry D, Leygraf C. Hydrogen peroxide toward enhanced oxide growth on titanium in PBS solution: Blue coloration and clinical relevance. J Biomed Mater Res 1996;30:393–402.
32. Lin HY, Bumgardner JD. In vitro biocorrosion of Ti-6Al-4V implant alloy by a mouse macrophage cell line. J Biomed Mater Res A 2004;68:717–724.
33. Lin HY, Bumgardner JD. Changes in surface composition of the Ti-6Al-4V implant alloy by cultured macrophage cells. App Surf Sci 2004;225:21–28.
34. Yokoyama K, Ogawa T, Fujita A, Asaoka K, Sakai J. Unpublished data.
35. Rondelli G, Vicentini B. Evaluation by electrochemical tests of the passive film stability of equiatomic Ni-Ti alloy also in presence of stress-induced martensite. J Biomed Mater Res 2000;51:47–54.
36. Huang HH. Corrosion resistance of stressed NiTi and stainless steel orthodontic wires in acid artificial saliva. J Biomed Mater Res A 2003;66:829–839.
37. Yokoyama K, Watabe S, Hamada K, Sakai J, Asaoka K, Nagumo M. Susceptibility to delayed fracture of Ni-Ti superelastic alloy. Mater Sci Eng A 2003;341:91–97.
38. Yokoyama K, Eguchi T, Asaoka K, Nagumo M. Effect of constituent phase of Ni-Ti shape memory alloy on susceptibility to hydrogen embrittlement. Mater Sci Eng A 2004;374:177–183.

39. Oshida Y, Sachdeva RCL, Miyazaki S. Microanalytical characterization and surface modification of TiNi orthodontic archwires. Biomed Mater Eng 1992;2:51–69.
40. Yokoyama K, Ogawa T, Fujita A, Asaoka K, Sakai J. Unpublished data.
41. Rondelli G, Vicentini B, Cigada A. The corrosion behaviour of nickel titanium shape memory alloys. Corros Sci 1990;30:805–812.
42. Shabalovskaya SA, Anderegg JW. Surface spectroscopic characterization of TiNi nearly equiatomic shape memory alloys for implants. J Vac Sci Technol A 1995;13:2624–2632.
43. Aziz-Kerrzo M, Conroy KG, Fenelon AM, Farrell ST, Breslin CB. Electrochemical studies on the stability and corrosion resistance of titanium-based implant materials. Biomaterials 2001;22:1531–1539.
44. Chu CL, Chung CY, Zhou J, Pu YP, Lin PH. Fabrication and characteristics of bioactive sodium titanate/titania graded film on NiTi shape memory alloy. J Biomed Mater Res A 2005;75:595–602.
45. Chu CL, Chung CY, Chu PK. Surface oxidation of NiTi shape memory alloy in a boiling aqueous solution containing hydrogen peroxide. Mater Sci Eng A 2006;417:104–109.
46. Wälivaara B, Lundström I, Tengvall P. An in-vitro study of H_2O_2-treated titanium surfaces in contact with blood plasma and a simulated body fluid. Clin Mater 1993;12:141–148.
47. Pan J, Liao H, Leygraf C, Thierry D, Li J. Variation of oxide films on titanium induced by osteoblast-like cell culture and the influence of an H_2O_2 pretreatment. J Biomed Mater Res 1998;40:244–256.
48. Wang XX, Hayakawa S, Tsuru K, Osaka A. Improvement of bioactivity of $H_2O_2/TaCl_5$-treated titanium after subsequent heat treatments. J Biomed Mater Res 2000;52:171–176.
49. Takemoto S, Yamamoto T, Tsuru K, Hayakawa S, Osaka A, Takashima S. Platelet adhesion on titanium oxide gels: Effect of surface oxidation. Biomaterials 2004;25:3485–3492.

Effects of Surface Oxide Films on Hydrogen Absorption and Mechanical Properties of Titanium

Kenzo Asaoka

Reprinted from
Dentistry in Japan Vol. 43
pp. 99–103

March, 2007

Dental Materials and Devices

Effects of Surface Oxide Films on Hydrogen Absorption and Mechanical Properties of Titanium

Kenzo Asaoka*

Dentistry in Japan
Vol. 43 pp. 99~103, March, 2007

Because the fracture of medical/dental devices made of Titanium (Ti) and Ti alloys by hydrogen embrittlement has been reported, the effects of surface oxide films on hydrogen absorption and the mechanical strength of Ti were studied. To form a surface oxide film, cp-Ti wires were annealed in ambient air at 800°C for 2h. Half of the specimens were immersed in a mixed solution of NaF and H_3PO_4 (APF). Some of the specimens were removed from the surface film by abrasion after heating and immersion in the APF solution. Thermal desorption spectroscopy (TDS) was carried out to detect ions/molecules released during heating from room temperature to 1,200°C in a high-vacuum vessel for the treated specimens. A high ion intensity was detected for hydrogen at $m/z = 2$; however, the ion intensities of the other ions/molecules were almost at the background level in the measurements in which the specimen did not undergo severe corrosion. The hydrogen concentration in the specimens related to the heat and chemical process was determined quantitatively, and found to be not significantly enhanced by the annealing or immersion in APF solution when the specimen formed the surface film with the annealing. The mechanical strength of Ti was decreased when the specimen, which was removed from the oxide film, was attacked by hydrogen, thereby decreasing its mechanical strength.

Key words: Titanium — Corrosion — Strength — Hydrogen — Oxide film

INTRODUCTION

Titanium (Ti) is an active metal. However, surface oxide films (TiO_2) provide corrosion resistance and biocompatibility to this metal. The surface of Ti, which had been worked or polished/grinded, has a noncrystal thin oxide film. This surface film is not adequate to protect against chemical reaction. When Ti is annealed in ambient air, the metal becomes covered with crystalline oxide films such as anatase and rutile, and its corrosion resistance is improved. However, the thickness of such oxide films rapidly increases at temperatures higher than 900°C, and flakes fall off as scales. It is recognized that the control of the surface film on Ti is very important for the development of corrosion-resistant alloys.[1-2]

In an electrochemical study, the corrosion of metal related with electric potential and pH is carried out using corrosion diagrams developed by Pourbaix.[3] In the thermodynamically stable region in water at 1 atm (1×10^5 Pa), Ti is in a passive state. However, Ti deteriorates in solutions containing fluoride ions.[4-6]

Thermal desorption spectroscopy (TDS) is a method of analyzing the ions released by quadrupole mass spectrometry (QMS) while heating a specimen in a high-vacuum vessel. This is a useful method of obtaining information on the ions absorbed or taken up by a specimen.[7] In this study, the release of ions/molecules from cp-Ti wires, annealed cp-Ti wires and cp-Ti wires, which were immersed in a fluoride-containing solution, were analyzed by TDS. The effects of annealing and immersion treatment in APF solution on the uptake or absorption of ions/molecules were determined. Moreover, the relationship between the surface oxide film and the degradation of the Ti substrate was discussed.

MATERIALS AND METHODS

Cp-Ti wires (TI-451414, Nilaco, Tokyo) with a diameter of 0.6mm were cut into specimens of 50mm length. The as-received wires were polished with #800-grit SiC paper and ultrasonically washed in acetone and distilled water for 15min each. The specimens were annealed at 800°C for 2h in ambient air in an electrical furnace. Some of the annealed specimens were immersed in an aqueous solution (pH5.0) of 2.0%

Accepted on October 2, 2006

* Department of Biomaterials and Bioengineering,
Institute of Health Biosciences,
The University of Tokushima Graduate School
3-18-15 Kuramoto-cho, Tokushima 770-8504

acidulated phosphate fluoride (APF; 2.0% NaF + 1.7% H_3PO_4) at 37°C. For half of the specimens, the surface oxide film was removed using abrasive paper, and the specimens were ultrasonically washed. The surface morphology of each specimen was observed by scanning electron microscopy (SEM). The specimen for TDS was arranged after annealing and immersion treatment in APF solution. Ions released from the specimens in a high-vacuum chamber (1.3×10^{-7} Pa) were measured by TDS (EMD-WA1000S/W: ESCO, Tokyo) during heating at 0.5°C/sec. The time interval for the detection of the released ions by QMS was 5 sec. Table 1 shows a list of the heat and immersion treatments of the specimens with their codes.

Tensile test was carried out at room temperature using an Instron-type machine (Autograph AG-100A, Shimadzu, Kyoto) at a strain rate of 1.7×10^{-3}/sec. Stress-strain curves were measured for three specimens with the same treatment. The fractured surface was observed by SEM.

RESULTS

1. As-received Ti specimen (A)

The surface morphology of A (as-received cp-Ti) showed scratches, which might have been caused by drawing the specimen through a die, along the longitudinal direction. In high-magnification photographs, tear cracks were observed. Specimen A was heated to 1,200°C (1st run), and cooled to room temperature in an evacuated chamber in the TDS equipment. After that, the specimen was reheated to 1,200°C (2nd run). Figure 1 shows the net ion intensity of the hydrogen ($m/z=2$) that was released from specimen A, that is, the data used was obtained subtracting the background data (2nd run) from the data of the 1st run. The integrated value of the intensity curve from

Table 1 Codes of specimens with heat and immersion treatments

Code	Heat and immersion treatments
A	As-received material: reference
B-1	Annealed at 800°C for 2 h
B-2	Surface film removed from B-1 by abrasion
C-1	B-1 immersed in APF solution for 30 days
C-2	Surface film removed from C-1 by abrasion
C-3	B-2 immersed in APF solution for seven days

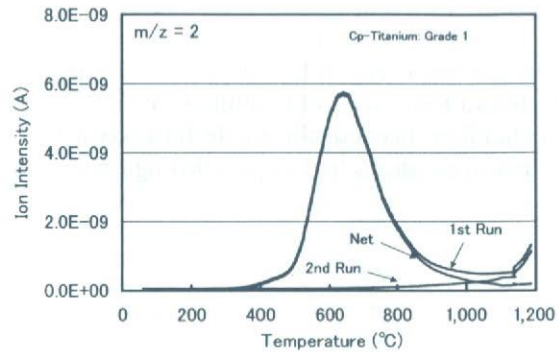

Fig. 1 Desorption curves of hydrogen ion intensities at $m/z=2$, released during heating of A by TDS
The vertical axis shows ion intensity and unit is ampere on the 10^{-9} order.

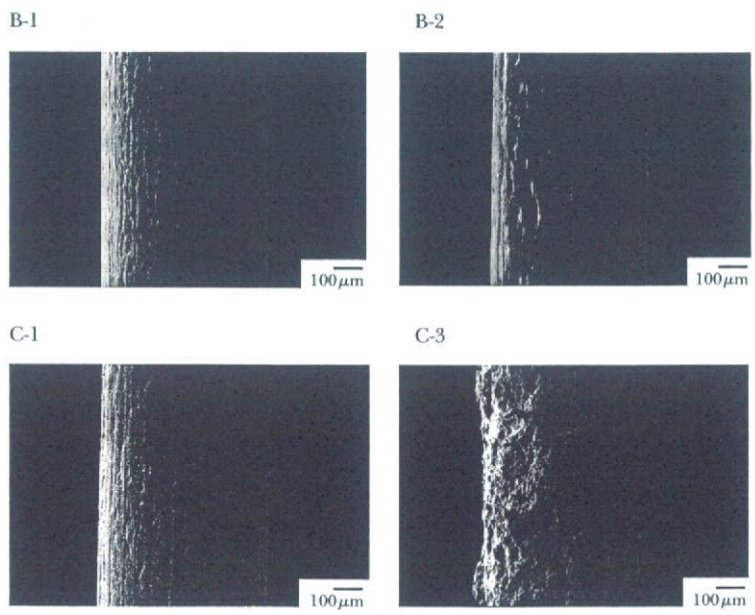

Fig. 2 Surface of specimens before tensile test
B-1: After annealing at 800°C for 2 h. B-2: After removing the surface oxide film from B-1 by abrasion.
C-1: After immersion of B-1 in APF solution for 30 days. C-3: After immersion of B-2 in APF solution for seven days.

room temperature to 1,000°C was compared with the reference data, and the number of hydrogen molecules released from specimen A was calculated to be 1.1×10^{17} for 10 mg. From this value, the hydrogen concentration in specimen A was calculated to be 37 mass ppm. Here, the hydrogen concentration can be calculated as {(mass of hydrogen) × (number of released ions)}/{(weight of specimen) × (Avogadro's number: 6.02×10^{23} amu/g)}.

2. Annealed specimens (B-1 and B-2)

The surface morphology of the annealed specimen B-1 was similar to that of specimen A from the SEM photo image graphs shown in Fig. 2. However, a thick surface oxide film was confirmed by visual inspection. With annealing at 800°C, the oxide film formed might be rutile and measured to be 9μm thick.[1] Figure 3 shows the ion intensity at m/z=2 for B-1 and B-2 compared with that of the reference specimen A. Here, B-2 is the oxide film removed from specimen B-1 by abrasion. For B-1, TDS measurements were repeated in four cycles of heating in the same evacuated chamber, because the oxide film was a barrier that hydrogen atoms had to pass through and hydrogen atoms remained in Ti after each of the cycles. The detected ion intensity of hydrogen at m/z=2 decreased depending on the number of heating cycles. However, the curve with the peak intensity was detected for B-2, which showed a similar curve to A (as-received cp-Ti). The onset temperature of the release of hydrogen was almost the same as that for A. These results indicate that the diffusion rate of hydrogen through the surface oxide film is extremely low, that is, the oxide film plays an important role in preventing the occlusion and dislodgement of hydrogen molecules. The calculated amounts of hydrogen released for B-1 and B-2 were calculated 33 ppm and 40 ppm (for four cycles of heating), respectively; these are almost equal to the amount of hydrogen released from specimen A. It was concluded that Ti did not take up hydrogen significantly during annealing.

3. Immersion in APF solution (C-1, C-2 and C-3)

The surface of C-1, which was annealed and immersed in APF solution, showed almost the same features as B-1, that is, no traces of typical chemical attacks were observed, as shown in Fig. 2. Figure 4 shows the results of TDS, that is, the curves of hydrogen at m/z=2 for

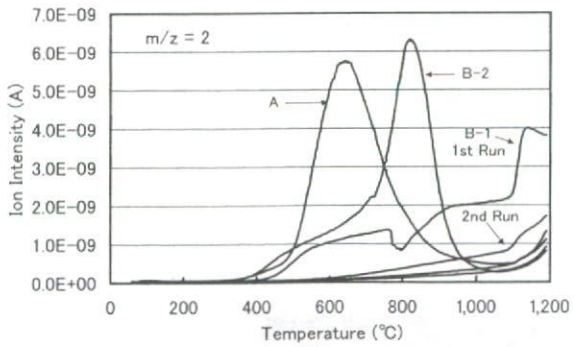

Fig. 3 Desorption curves of hydrogen ion intensities at m/z=2, released during heating of A, B-1 and B-2 determined by TDS

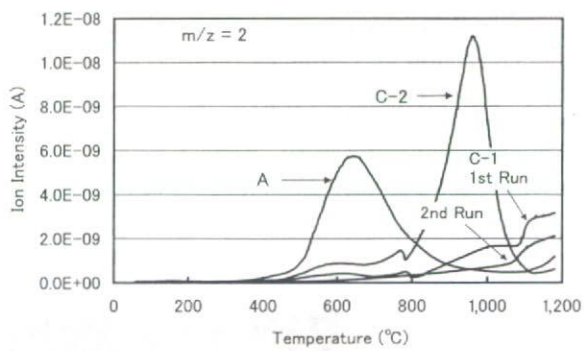

Fig. 4 Desorption curves of hydrogen ion intensities at m/z=2 released during heating of A, C-1 and C-2 determined by TDS

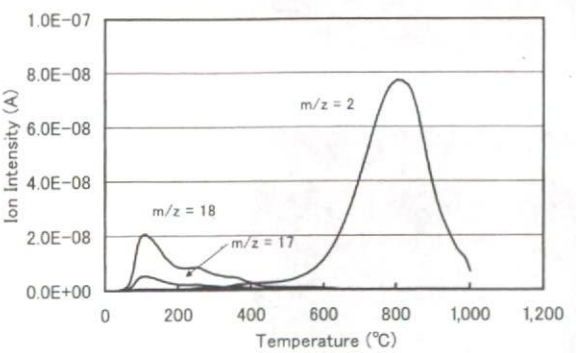

Fig. 5 Desorption curves of hydrogen ion and water ions at m/z=2, 17 and 18 for C-3 during heating

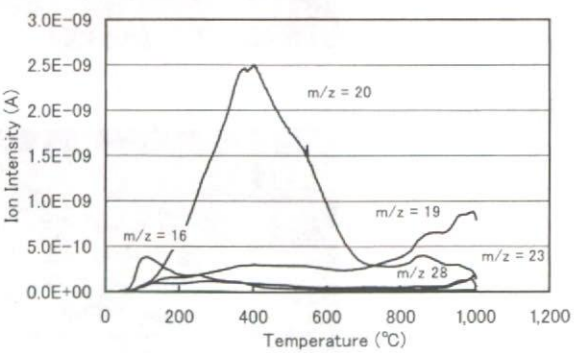

Fig. 6 Desorption curves of ion intensities at m/z=16, 19, 20, 23 and 28 for C-3 during heating

The other ion intensities were detected at the background level in the measurement.

C-1 and C-2 are shown in comparison with that for specimen A. The curves for C-1, which was covered with the oxide film, show that ion intensity increases as temperature increases. The ion intensity was low for the 2nd run compared with that for the 1st run, because the specimen had a lower hydrogen concentration during the 1st run as a result of desorption. The $m/z=2$ curve for C-2, in which the oxide film was removed after immersion in APF solution, shows a peak similar to those of specimen A and B-2. However, the peak temperature of C-2 is higher than those of A and B-2. The hydrogen concentrations calculated were 26 and 47 ppm for C-1 and C-2, respectively. This result shows that no significant increase in the rate of hydrogen uptake for the specimens with an oxide film, which was formed by annealing, was detected with the immersion in APF solution.

The surface of C-3, in which the surface film was removed after the annealing and immersion in APF solution for seven days, was markedly attacked by APF solution, and pores were observed on the surface as shown in Fig. 2. Figure 5 shows the ion intensity curve for C-3 by TDS. The ion intensity at $m/z=17$ and 18, which were related to the ions of water molecules, were high at temperatures lower than 400°C, and at temperatures higher than 400°C, that of hydrogen ($m/z=2$) was extremely high. The amount of hydrogen calculated was 864 ppm, which is 20 times higher than those of the specimens with the oxide film formed by annealing. Not only hydrogen and water, but also fluoride and sodium ions, which are the components of APF solution, were detected at higher intensities than background levels. The peak ion intensities related to fluorine ($m/z=20$ (HF) and 19 (F)) were detected to be the order of 10^{-9} A, as shown in Fig. 6. The concentrations of detected hydrogen for the Ti specimens are listed in Table 2.

Table 2 Concentration of hydrogen in the specimen with various treatments

Code	Number of Hydrogen molecules/10 mg	ppm
A	1.1×10^{17}	37
B-1	9.8×10^{16}	33
B-2	1.2×10^{17}	40
C-1	7.9×10^{16}	26
C-2	1.4×10^{17}	47
C-3	2.6×10^{18}	864

4. Tensile strength

Figure 7 shows the fractography results of the specimens. The ultimate tensile strength of the as-received specimen A was 680 MPa, because the wire had been formed by hard-cold work deformation. Because of the annealing at 800°C for 2h (B-1), the strength decreased to 370 MPa. These results agree with the data for grade 1 Ti.[8] Tensile fracture strain decreased from 14% to 10% because local cracks formed in the surface oxide film, which was a hard but brittle structure, in the early stage of the tensile test. These local cracks developed throughout the Ti matrix, and caused fracturing. For B-2, in which the surface film was removed by abrasion, many surface cracks formed uniformly in the surface layer of B-2 as shown in Fig. 7. The tensile strength was almost equal to that of B-1; however, the fracture strain of B-1 was almost equal to that of the as-received wire A. After

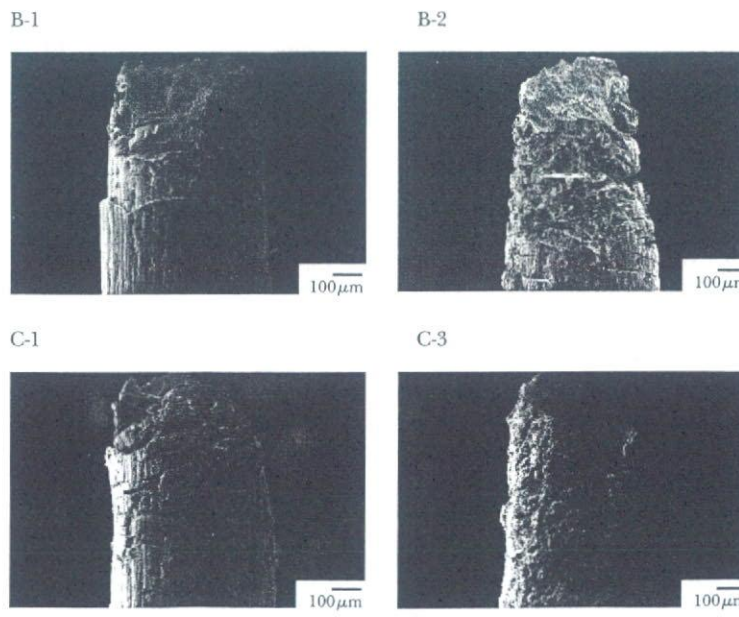

Fig. 7 Fractured surface of specimens after tensile test for each specimen shown in Fig. 2

the immersion in APF solution, the specimen with an oxide film (C-1) showed almost no corrosion attack damage as shown in an SEM photograph, and hydrogen concentration showed no increase. The strength and fracture strain showed no decreases. However, C-3, which was immersed in APF solution after the surface film abrasion, showed excessive corrosion attack damage as shown in Fig. 2. The strength of C-3 markedly decreased to 260 MPa. However, elongation rate increased to 20%. These results suggest that hydrogen absorption and strength degradation are accelerated by the corrosion of the surface oxide film. This may lead to the fracture of devices in high-stress environments.

DISCUSSION

Hydrogen, oxygen, nitrogen and carbon are interstitial impurity atoms in Ti. They increase the strength of Ti by solid solution hardening, except hydrogen. The maximum solubility of hydrogen in α-Ti is extremely low. Hydride formation, which is brittle phase, takes place when hydrogen concentration in Ti exceeds the solubility limit. From this, cp-Ti, which contains higher than 150–200 ppm hydrogen, loses its ductility in high-stress environments, resulting in increased notch sensitivity. This phenomenon is known as hydrogen embrittlement.[9] The solubility of hydrogen in cp-Ti, which is used as an implant material, is standardized to be hydrogen content lower than 150 ppm, or 100 ppm for billet.[10]

A titanium oxide layer, a few nanometers thick, is generated when a metal surface is exposed to ambient air by cutting or grinding. This oxide layer exerts a protective action, thereby conferring a high corrosion resistance on Ti. However, this corrosion resistance is not adequate for use in severely corrosive environments such as a fluoride-ion-containing solution. From the TDS curves for hydrogen of the specimen with an oxide film, the rate of hydrogen diffusion through titanium oxide is extremely low. The surface film traps released hydrogen. Titanium oxide (rutile) plays an important role in preventing Ti from hydrogen uptake. The results of immersing C-3 in APF solution show that the rate of hydrogen uptake is 20-fold the initial hydrogen concentration during a 7-day immersion. Because Ti is an active metal, water, fluoride and sodium ions were detected in C-3. The presence of hydrogen, which is absorbed during working and cleaning, is the most serious problem for the use of Ti. However, the hydrogen content in Ti increases in biological structures that use medical devices. For example, the hydrogen embrittlement of superelastic Ni-Ti orthodontic wire and Ti dental implant have been reported.[11,12] The reason for the fracture is inferred to be the insufficient thickness of the oxide film that protects hydrogen uptake in the mouth. Thus, it is important that the formation of oxide films such as rutile and anatase is enhanced to increase longevity of medical and dental devices.

Acknowledgements

I gratefully acknowledge the kind assistance of Mr. Kunimitsu Maejima, ESCO, Ltd., for his technical assistance, expertise and advice.

REFERENCES

1) Am Soc Met: Heat treating of titanium and titanium alloys. In: *ASM Metals Handbook Vol. 4* (9th ed.). ASM, Ohio, 1981, pp. 754–774.
2) Watari, F. and Nishimura, F.: Oxygen solid solution hardening in titanium by heat treatment. *J. J. Dent. Mater.* **10**: 266–274, 1991. (in Japanese with English abstract)
3) Schmets, J., Muylder, J.V. and Pourbaix, M.: Titanium. In: *Atlas of Electrochemical Equilibria in Aqueous Solutions.* National Association of Corrosion Engineers, Houston, 1974, pp. 213–221.
4) Kononen, M.H., Lavonius, E.T. and Kivilahti, J.K.: SEM observations on stress corrosion cracking of commercially pure titanium in a topical fluoride solution. *Dent. Mater.* **11**: 269–272, 1995.
5) Reclaru, L. and Meyer, J.M.: Effects of fluorides on titanium and other dental alloys in dentistry. *Biomater.* **19**: 85–92, 1998.
6) Schiff, N. *et al.*: Influence of fluoride content and pH on the corrosion resistance of titanium and its alloys. *Biomater.* **23**: 1995–2002, 2002.
7) Asaoka, K. and Maejima, K.: Effect of surface oxide films on degradation of titanium by thermal desorption spectroscopy. *J. J. Dent. Mater.* **24**: 439–445, 2005. (in Japanese with English abstract)
8) Breme, H.J., Biehl, V. and Helsen, J.A.: Metals and implants. In: *Metals As Biomaterials* (ed. by Helsen, J.A. and Breme, H.J.). John Wiley & Sons, Chicago, 1998, pp. 53–58.
9) Williams, D.N.: The hydrogen embrittlement of titanium alloys. *J. Inst. Met.* **91**: 147–152, 1962.
10) ASTM Standards: F67-00 Standard specification for unalloyed titanium, for surgical implant applications. In: *Annual Book of ASTM Standards. Vol. 13.01.* ASTM International, PA, 2005, pp. 43–46.
11) Yokoyama, K., Hamada, K., Moriyama, K. and Asaoka, K.: Degradation and fracture of Ni-Ti superelastic wire in an oral cavity. *Biomater.* **22**: 2257–2262, 2001.
12) Yokoyama, K., Ichikawa, T., Murakami, Y., Miyamoto, Y. and Asaoka, K.: Fracture mechanisms of retrieved titanium screw thread in dental implant. *Biomater.* **23**: 2456–2465, 2002.

Reprint requests to:
Dr. Kenzo Asaoka
Department of Biomaterials and Bioengineering,
Institute of Health Biosciences,
The University of Tokushima Graduate School
3-18-15 Kuramoto-cho, Tokushima 770-8504, Japan
E-mail: asaoka@dent.tokushima-u.ac.jp

Available online at www.sciencedirect.com
ScienceDirect
Scripta Materialia 57 (2007) 393–396
Scripta MATERIALIA
www.elsevier.com/locate/scriptamat

Hydrogen absorption and thermal desorption behaviors of Ni–Ti superelastic alloy subjected to sustained tensile-straining test with hydrogen charging

Ken'ichi Yokoyama,[a,*] Miho Tomita,[b] Kenzo Asaoka[a] and Jun'ichi Sakai[b]

[a] *Department of Biomaterials and Bioengineering, Institute of Health Biosciences, The University of Tokushima Graduate School, 3-18-15 Kuramoto-cho, Tokushima 770-8504, Japan*

[b] *Department of Materials Science and Engineering, Waseda University, 3-4-1 Okubo, Shinjuku-ku, Tokyo 169-8555, Japan*

Received 7 March 2007; revised 25 April 2007; accepted 5 May 2007
Available online 6 June 2007

The hydrogen absorption and thermal desorption behaviors of Ni–Ti superelastic alloy subjected to a sustained tensile-straining test with cathodic hydrogen charging have been investigated. Under an applied strain in the presence of the martensite phase, hydrogen absorption is markedly enhanced and the amount of desorbed hydrogen, particularly at low temperatures, is increased. In addition, the hydrogen diffusion distance in the specimen increases.
© 2007 Acta Materialia Inc. Published by Elsevier Ltd. All rights reserved.

Keywords: Ni–Ti; Superelastic alloy; Hydrogen embrittlement; Thermal desorption analysis

Hydrogen embrittlement of Ni–Ti superelastic alloy is considered to be sensitive to stress/strain or phase transformation [1–8]. Upon tensile loading, hydrogen-charged Ni–Ti superelastic alloy fractures as a result of stress-induced martensite transformation [5–8]. From the results of a sustained tensile-loading test with hydrogen charging, we have demonstrated that when the applied stress exceeds the critical stress for martensite transformation, the amount of absorbed hydrogen increases markedly; hence, the time for the alloy to fracture probably becomes short [9,10]. For a sustained tensile-loading test, however, the hydrogen absorption behavior during the stress-induced martensite and reverse transformation cannot be investigated. In addition, Ni–Ti superelastic alloy is widely used under sustained straining conditions rather than under sustained loading conditions [11–14]. Therefore, to further understand the hydrogen embrittlement of the alloy, the hydrogen absorption and thermal desorption behaviors under an applied strain during stress-induced martensite and reverse transformation must be examined. The thermal desorption behavior of hydrogen allows hydrogen in various materials to be characterized as diffusive hydrogen, hydrogen trapped in defects or hydrogen in solution [15–22].

The objective of the present study is to investigate the hydrogen absorption and thermal desorption behaviors of Ni–Ti superelastic alloy subjected to a sustained tensile-straining test with cathodic hydrogen charging.

A commercial Ni–Ti superelastic alloy (Ni 55 mass%, Ti balance) wire with a diameter of 0.50 mm was cut into 120 mm long specimens. The specimens were polished with 600-grit SiC paper and ultrasonically cleaned with acetone for 5 min.

A sustained tensile-straining test with hydrogen charging was carried out using an Instron-type machine at room temperature (25 ± 2 °C) with specimens 50 mm in length immersed in 150 ml of 0.9% NaCl aqueous solution. The gauge length of each specimen was 80 mm. Strain was calculated from the displacement of the crosshead and the initial gauge length. The conditions of cathodic hydrogen charging were a current density of 10 A m^{-2} for 2 h. After applying a sustained-strain, the start of hydrogen charging was 30 s.

Hydrogen thermal desorption analysis (TDA) was performed in vacuum at 10^{-6} Pa using a quadrupole mass spectrometer (ULVAC, Kanagawa, Japan). Sampling was conducted at 30 s intervals at a linear heating rate of 100 °C h^{-1} up to 600 °C. To account for experimental errors, the TDA was carried out at least twice.

* Corresponding author. Tel.: +81 88 633 7334; fax: +81 88 633 9125; e-mail: yokken@dent.tokushima-u.ac.jp

1359-6462/$ - see front matter © 2007 Acta Materialia Inc. Published by Elsevier Ltd. All rights reserved.
doi:10.1016/j.scriptamat.2007.05.002

After hydrogen charging, the start of TDA was 60 min. The amount of desorbed hydrogen was defined as the integrated peak intensity. The amount of absorbed hydrogen was calculated by subtracting the amount of predissolved hydrogen (10 mass ppm). To evaluate hydrogen distribution in a hydrogen-charged specimen, the surface of the specimens was carefully ground to various thicknesses with 180-grit SiC paper and measured using a micrometer caliper immediately before TDA. The local concentration of hydrogen was calculated from the ratio of the sectional areas and the amount of desorbed hydrogen from the ground specimens.

The amounts of hydrogen absorbed by the Ni–Ti superelastic alloy charged with hydrogen under various applied strains obtained by TDA are shown in the stress–strain curve in Figure 1. Hereafter, the uppercase letters in the figures indicate applied sustained-strain points, as shown in Figure 1. In our previous TDA results [23], the scatter of the amount of absorbed hydrogen of the alloy without an applied strain (point A) is at most 10 mass ppm. In the present study, therefore, the experimental errors are probably within 5–10%. On loading, under the applied strains up to the middle of the stress plateau due to stress-induced martensite transformation (point C), the amount of absorbed hydrogen only slightly increased compared with that without an applied strain (point A); the increment in the amount of absorbed hydrogen was at most 10–20 mass ppm. This increment in the amount of absorbed hydrogen might be caused by the increment in the number of hydrogen trap sites induced by the elastic deformation of the B2 parent phase. When the applied strain exceeds the later stage of the stress plateau due to martensite transformation (point D), the amount of absorbed hydrogen increased markedly (approximately 350 mass ppm). Under the applied strain in the elastic deformation region of the B19′ martensite phase (point E), the hydrogen absorption behavior approximately corresponds to that under the sustained tensile-loading test wherein the applied stress exceeds the critical stress for the martensite transformation [9]. Under the applied strain in the plastic deformation region of the martensite phase (point F), the amount of absorbed hydrogen maximally increased (approximately 400 mass ppm). This increment in the amount of absorbed hydrogen is presumably caused by the increment in the number of hydrogen trap sites as induced by plastic deformation [24].

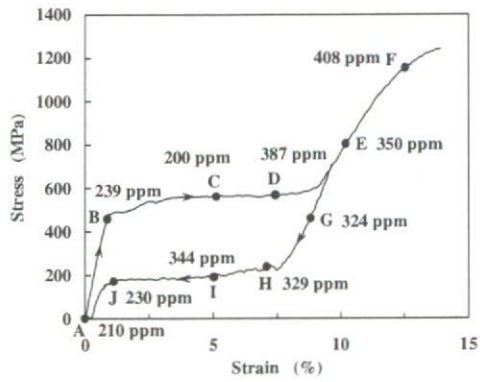

Figure 1. Relationship between applied strain points on the stress–strain curve of Ni–Ti superelastic alloy and the amounts of absorbed hydrogen obtained from TDA. The letters in the figure indicate applied strain points. Strain is calculated from elongation (displacement of crosshead) and initial gauge length.

On unloading from point E, an increment in the amount of absorbed hydrogen was observed under the applied strains up to the middle of the stress plateau due to reverse transformation (point I). Under the applied strains from points G to I, although the applied stress was lower than the critical stress for the martensite transformation, the amount of absorbed hydrogen increased (approximately 350 mass ppm), as compared with that without an applied strain (point A). From a practical viewpoint, it should be emphasized that hydrogen absorption is markedly enhanced under the applied strains at the stress plateau due to reverse transformation. The amount of absorbed hydrogen only slightly increased under the applied strain at the later stage of the stress plateau due to reverse transformation (point J), as compared with that without an applied strain (point A).

The present results with the Ni–Ti superelastic alloy suggest that hydrogen absorption is enhanced by the existence of the martensite phase rather than by an applied stress level. This is consistent with the previous finding that when Ni–Ti shape memory alloys with different phases are charged, the martensite phase can be observed to enhance hydrogen absorption [24]. Burch and Mason [25] reported that the thermoelastic martensite transformation enhances the solubility of hydrogen in Ti–Ni alloy at high temperature. For $Ti_{50-x}Zr_xNi_{50}$ (at.%) alloys, Cuevas et al. [26] reported that the thermoelastic martensitic structure is able to store a much higher amount of hydrogen than the austenitic one. With regard to the reason for the inhibition of the enhancement of hydrogen absorption under the applied strain at point C, the relationship between the stress plateau region of the stress–strain curves and the existence of the martensite phase must be examined carefully [27–31]. Shaw and Kyriakides [27,28] reported that the stress-induced phase transformation of Ni–Ti alloy results in an inhomogeneous deformation: the nucleation of the martensite phase in a uniform parent phase region is associated with a stress peak on loading, whereas the nucleation of a parent phase in a uniform martensite phase region is associated with a stress valley on unloading. Therefore, at the center of the specimen (the hydrogen charging region), it appears that the martensite phase does not exist under the applied strain at point C, although the martensite phase exists under the applied strain at point I. The quantitative relationship between the volume fraction of the martensite phase and the amount of hydrogen absorption should be investigated further.

Figure 2 shows the hydrogen thermal desorption curves of the Ni–Ti superelastic alloy under various applied strains. Hydrogen desorption was observed from room temperature to 400 °C irrespective of the applied strain points. For the specimens charged at points A, B, C and J, the primary peak was observed at approximately 270 °C; the shoulder of the primary peak was observed at 150–200 °C. For the specimen charged

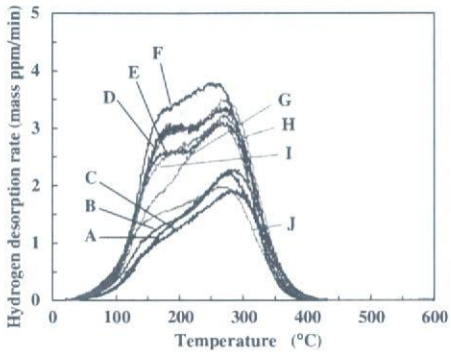

Figure 2. Hydrogen thermal desorption curves of specimen charged with hydrogen under various applied strains. The letters in the figure indicate applied strain points (see Fig. 1).

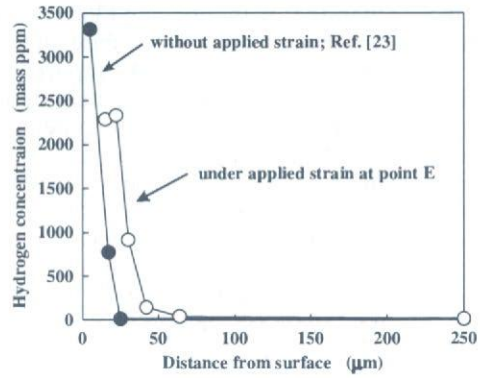

Figure 4. Hydrogen concentration evaluated by TDA as function of distance from surface of hydrogen-charged specimens without applied strain and under applied strain at point E (see Fig. 1).

under the applied strains from points D to I, the amount of hydrogen desorbed at low temperatures increased markedly, although the amount of the primary peak increased. From the results of our previous study [23], the hydrogen desorption behavior at low temperatures appears to be particularly involved in the hydrogen embrittlement of the alloy. It seems that the marked increase in the amount of hydrogen desorbed at low temperatures readily results in hydrogen embrittlement.

Figure 3 shows the hydrogen thermal desorption curves of the surface-ground specimens under the applied strain in the elastic deformation region of the martensite phase (point E). The amount of desorbed hydrogen decreased with decreasing diameter of the ground specimen. The amount of desorbed hydrogen for the 0.35 mm diameter specimen was almost the same as that for the non-charged specimen; hence, the charged hydrogen exists within at most 75 μm from the surface of the specimen. From our previous results for the specimen charged without an applied strain (parent phase) [23], the charged hydrogen exists within at most 25 μm from the surface of the specimen. The hydrogen diffusion rate in the martensite phase (B19′) may be higher than that in the parent phase (B2). The longer diffusion distance of hydrogen in the martensite phase is probably one of the reasons why hydrogen embrittlement occurs readily under the applied stresses above the stress-induced martensite transformation, i.e. under the existence of the martensite phase [9,10].

Figure 4 shows the hydrogen concentration and distribution of the hydrogen-charged specimens without an applied strain, as reported previously [23] and under an applied strain in the elastic deformation region of the martensite phase (point E), as evaluated from Figure 3. The hydrogen concentration was more than 2000 mass ppm in the vicinity of the surface of the specimen under an applied strain. This hydrogen concentration is enough to result in the pronounced degradation of the mechanical properties of the Ni–Ti superelastic alloy. The effects of hydrogen concentration and distribution on the mechanical properties of the alloy have been described in our previous articles [23,32].

Figure 5 shows the hydrogen thermal desorption curve of the hydrogen-charged specimen under an applied strain in the elastic deformation region of the martensite phase (point E) followed by aging for 240 h at room temperature in air without an applied strain. Upon aging, the amount of hydrogen desorbed at low temperatures decreased, in accordance with the desorption in specimens charged without an applied strain, as reported previously [23,32]. The amount of desorbed hydrogen in the aged specimens (383 mass ppm) was

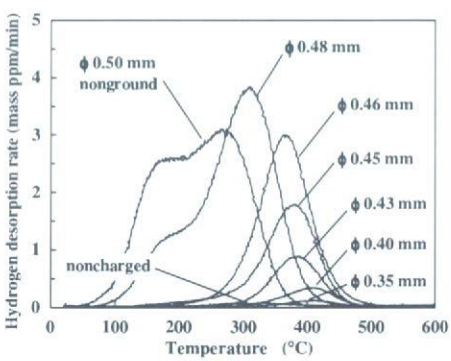

Figure 3. Hydrogen thermal desorption curves of surface-ground specimens charged with hydrogen under applied strain at point E (see Fig. 1). The numerical values in this figure indicate the diameters of the ground specimens.

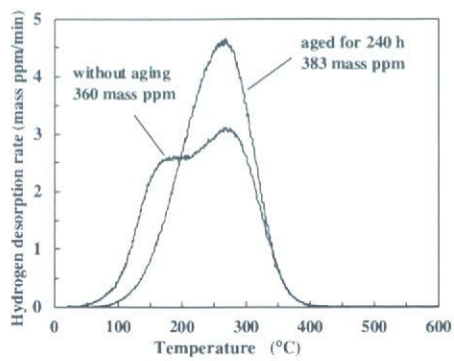

Figure 5. Representative hydrogen thermal desorption curves of hydrogen-charged specimen under applied strain at point E (see Fig. 1), aged for 240 h at room temperature in air. The numerical values in this figure indicate the amount of desorbed hydrogen.

slightly higher than that without aging (360 mass ppm); it appears that hydrogen does not diffuse out during aging at room temperature in air. As reported previously [23], some hydrogen molecules that desorb at low temperatures probably diffuse out under reduced pressure before TDA, although hydrogen rarely diffuses out during aging at room temperature under atmospheric pressure. Upon aging, it is likely that hydrogen desorbed at low temperatures diffuses toward the center of the specimen and becomes stable; hydrogen rarely diffuses out under reduced pressure. Thus, for the specimen immediately after hydrogen charging, the amount of desorbed hydrogen obtained by TDA appears to be slightly smaller than the actual value.

The hydrogen state in the parent phase of the Ni–Ti superelastic alloy has been described in our previous articles [23,32]. In the present TDA results, there is no distinct evidence that the hydrogen states are different between the parent and martensite phases. Nevertheless, the hydrogen desorption behavior at low temperatures and the hydrogen distribution are changed for the specimen charged in the presence of the martensite phase; hence, the hydrogen state is possibly changed in association with the martensite phase. Further studies are needed to clarify this point.

This study was supported in part by a Grant-in-Aid for Young Scientists (B) (17791397) and a Grant-in-Aid for Scientific Research (C) (18560702) from the Ministry of Education, Culture, Sports, Science and Technology, Japan.

[1] N. Wade, Y. Adachi, Y. Hosoi, Scripta Metall. Mater. 24 (1990) 1051.
[2] Y. Adachi, N. Wade, Y. Hosoi, J. Jpn. Inst. Met. 54 (1990) 525.
[3] T. Hoshiya, S. Den, H. Katsuta, H. Ando, J. Jpn. Inst. Met. 56 (1992) 747.
[4] T. Asaoka, H. Yamashita, H. Saito, Y. Ishida, J. Jpn. Inst. Met. 57 (1993) 1123.
[5] K. Yokoyama, K. Hamada, K. Moriyama, K. Asaoka, Biomaterials 22 (2001) 2257.
[6] K. Yokoyama, K. Kaneko, K. Moriyama, K. Asaoka, J. Sakai, M. Nagumo, J. Biomed. Mater. Res. A 65A (2003) 182.
[7] K. Yokoyama, T. Ogawa, K. Asaoka, J. Sakai, M. Nagumo, Mater. Sci. Eng. A 360 (2003) 153.
[8] T. Ogawa, K. Yokoyama, K. Asaoka, J. Sakai, Mater. Sci. Eng. A 393 (2005) 239.
[9] K. Yokoyama, S. Watabe, K. Hamada, J. Sakai, K. Asaoka, M. Nagumo, Mater. Sci. Eng. A 341 (2003) 91.
[10] K. Yokoyama, K. Kaneko, K. Moriyama, K. Asaoka, J. Sakai, M. Nagumo, J. Biomed. Mater. Res. A 69A (2004) 105.
[11] K. Otsuka, C.M. Wayman (Eds.), Shape Memory Materials, Cambridge University Press, Cambridge, 1998.
[12] J. Van Humbeeck, Mater. Sci. Eng. A 273–275 (1999) 134.
[13] T. Duerig, A. Pelton, D. Stöckel, Mater. Sci. Eng. A 273–275 (1999) 149.
[14] N.B. Morgan, Mater. Sci. Eng. A 378 (2004) 16.
[15] W.Y. Choo, J.Y. Lee, Metall. Trans. A 13A (1982) 135.
[16] K. Ono, M. Meshii, Acta Metall. Mater. 40 (1992) 1357.
[17] A. Turnbull, R.B. Hutchings, D.H. Ferriss, Mater. Sci. Eng. A 238 (1997) 317.
[18] S.W. Smith, J.R. Scully, Metall. Mater. Trans. A 31A (2000) 179.
[19] M. Nagumo, M. Nakamura, K. Takai, Metall. Mater. Trans. A 32A (2001) 339.
[20] K. Takai, R. Watanuki, Iron Steel Inst. Jpn. Int. 43 (2003) 520.
[21] T. Nishiue, Y. Kaneno, H. Inoue, T. Takasugi, J. Alloy. Compd. 364 (2004) 214.
[22] F.G. Wei, K. Tsuzaki, Metall. Mater. Trans. A 37A (2006) 331.
[23] M. Tomita, K. Yokoyama, K. Asaoka, J. Sakai, Mater. Sci. Eng. A, in press, doi:10.1016/j.msea.2007.04.104.
[24] K. Yokoyama, T. Eguchi, K. Asaoka, M. Nagumo, Mater. Sci. Eng. A 374 (2004) 177.
[25] R. Burch, N.B. Mason, J. Chem. Soc., Faraday Trans. I 75 (1979) 561.
[26] F. Cuevas, M. Latroche, P. Ochin, A. Dezellus, J.F. Fernández, C. Sánchez, A. Percheron-Guégan, J. Alloy. Compd. 330–332 (2002) 250.
[27] J.A. Shaw, S. Kyriakides, J. Mech. Phys. Solids 43 (1995) 1243.
[28] J.A. Shaw, S. Kyriakides, Acta Mater. 45 (1997) 683.
[29] R. Vaidyanathan, M.A.M. Bourke, D.C. Dunand, Acta Mater. 47 (1999) 3353.
[30] K. Gall, H. Sehitoglu, Int. J. Plast. 15 (1999) 69.
[31] L.C. Brinson, I. Schmidt, R. Lammering, J. Mech. Phys. Solids 52 (2004) 1549.
[32] K. Yokoyama, T. Ogawa, K. Takashima, K. Asaoka, J. Sakai, Mater. Sci. Eng. A, in press, doi:10.1016/j.msea.2007.02.102.

J Periodont Res 2007; 42; 114–118
All rights reserved

Copyright © Blackwell Munksgaard Ltd
JOURNAL OF PERIODONTAL RESEARCH
doi:10.1111/j.1600-0765.2006.00922.x

Dense fimbrial meshwork enhances *Porphyromonas gingivalis* adhesiveness: a scanning electron microscopic study

H. Hongo[1], H. Takano[2], M. Morita[1]
Departments of [1]Oral Health Science and [2]Functional Morphology, Hokkaido University Graduate School of Dental Medicine, Sapporo, Japan

Hongo H, Takano H, Morita M. Dense fimbrial meshwork enhances Porphyromonas gingivalis *adhesiveness: a scanning electron microscopic study. J Periodont Res 2007; 42: 114–118. © Blackwell Munksgaard 2006*

Background and Objective: The aim of this study was to determine how the fimbriae of *Porphyromonas gingivalis* function in plaque formation.

Material and Methods: We used scanning electron microscopy to examine aggregates and hemaggregates of fimbria-rich ATCC33277 (parent) and fimbra-poor OZ6301C (*pgmA*-knockout, mutant) strains of *P. gingivalis*. We also assessed the hemagglutination activity of the two strains as an indicator of *P. gingivalis* adhesiveness.

Results: Aggregates of *P. gingivalis* were composed of bacterial chains and clusters. Rich fimbriae projecting from cells of the parent strain tended to bunch and form a dense meshwork among bacterial cells. In contrast, cells of the mutant strain projected fewer fimbriae and the meshwork was looser. Hemaggregates including cells of the parent strain contained a detached, dense fimbrial meshwork that adhered to erythrocytes. Hemaggregates comprising cells of the mutant strain included bacterial chains and clusters that adhered to erythrocytes by shorter fimbriae than those of the parent strain. The hemagglutination titer of the parent strain was 10-fold higher than that of the mutant strain, although the number of fimbriae per cell of the parent strain was only double that of the mutant strain.

Conclusion: The results indicate that *P. gingivalis* adhesiveness is prominently enhanced by the dense fimbrial meshwork. Thus, the virulence of *P. gingivalis* is increased by the presence of rich fimbriae.

Dr Hirohisa Hongo, Department of Oral Health Science, Hokkaido University Graduate School of Dental Medicine, Kita 13 Nisi 7, Kita-ku, Sapporo 060-8586, Japan
Tel: +81 11 7064256
Fax: +81 11 7064918
e-mail: hhongo@den.hokudai.ac.jp

Key words: fimbriae; meshwork; *Porphyromonas gingivalis*; scanning electron microscopy

Accepted for publication May 26, 2006

Porphyromonas gingivalis is a gram-negative anaerobic rod that is usually detected in the periodontal pockets of patients with severe periodontitis (1). Lipopolysaccharide, released from the cell membranes of dead *P. gingivalis* in periodontal pockets, activates osteoclasts to resorb alveolar bone (2,3).

P. gingivalis induces alveolar bone resorption by adhering to the subgingival mucosa where it forms aggregates with gram-positive aerobic bacteria (4). Such aggregates stimulate neutrophils and lymphocytes to induce inflammation in the subgingival mucosa, allowing *P. gingivalis* to invade periodontal pockets further (5). Thereafter, *P. gingivalis* adheres to the cementum adjacent to alveolar bone, where osteoclasts stimulated by lipopolysaccharide released from dead *P. gingivalis* cause alveolar bone resorption (6).

Fimbriae are thought to not only mediate initial *P. gingivalis* adherence to the oral mucosa, but also to contribute to its colonization in subgingival pockets (7). Watanabe *et al.* (8) identified a close correlation between the number of fimbriae and the adhesiveness of *P. gingivalis* to

human oral mucosal epithelial cells and fibrocytes *in vitro*. Du *et al.* (9) proved biochemically that fimbriae and hemagglutinating adhesin mediate the adhesion of *P. gingivalis* to epithelial cells. Thus, physiological and biochemical findings both show that fimbrial adhesiveness and fimbria are involved in hemagglutination. However, morphological images, obtained by scanning electron microscopy (SEM), showing how *P. gingivalis* works in plaques and hemaggregates have not been published.

To visualize the function of *P. gingivalis* fimbria using SEM images, we examined cell aggregates and hemaggregates comprising *P. gingivalis* of parent and mutant strains that are fimbria-rich and fimbria-poor, respectively (10). The hemagglutination titers of both strains were also assessed to determine the relationship between fimbrial density and bacterial adhesiveness.

Material and methods

Strains

P. gingivalis ATCC33277 (parent strain) was obtained from the American Type Culture Collection (Rockville, MD, USA), and the OZ6301C (*pgmA*-knockout, mutant) was supplied by Aichi Gakuin University (Aichi, Japan). The *pgmA* gene of ATCC33277 (11) is inactivated in OZ6301C by Fletcher's DNA cassette that is erythromycin resistant (12). Strain OZ6301C expresses about half of the amount of fimbrilin found in ATCC33277 (10).

Method of incubation

The bacteria were suspended in 0.5 ml of Brain–Heart infusion (BHI) broth (Difco, Detroit, MI, USA) diluted to 50% of the standard concentration. One drop of the suspension medium was streaked onto plates containing Brucella agar medium (Kyokutou, Tokyo, Japan) and the plates were incubated under anaerobic conditions at 37°C.

To confirm the effectiveness of the DNA cassette, the *pgmA*-knockout strain was incubated under anaerobic conditions for 3 d at 37°C on agar media containing erythromycin (final concentration, 20 μg/ml). Pieces of colonies scraped from plates using an inoculating loop were mixed with 300 ml of GAM bouillon (Nissui, Tokyo, Japan). Flasks containing parent and mutant strains were incubated for 3.0–3.5 and 4.0–4.5 d, respectively. The mutant strain grew more slowly than the parent strain, and was incubated for 1 d longer than the parent strain to equalize the amount of aggregates of both. We incubated parent and mutant strains 23 and 12 times, respectively, to generate the data shown here.

Preparation of *P. gingivalis* cells for SEM

Flasks containing mutant and parent *P. gingivalis* aggregates in GAM bouillon were gently shaken to form homogeneous cell suspensions of about the same color.

One drop of each suspension was removed using a sterilized chopstick and placed on silane-coated 7-mm^2 glass slides. After 10 min, the slides were gently immersed in Petri dishes containing 0.02 M cacodylate buffer (pH 7.4), 0.15 M NaCl and 1% glutaraldehyde. The samples were fixed for 5 h, dehydrated in a graded series of ethanol, immersed in isoamyl acetate, dried in a critical point dryer, coated with osmium vapor for 1 s using an osmium plasma coater (Nippon Laser, Tokyo, Japan) and observed by SEM (S4500; Hitachi, Tokyo, Japan). We initially selected fields where the bacterial cells were intact at low magnification, and then photographed them at 5×10^4 magnification. Bacterial cells were considered intact or damaged when the fimbriae were rich and long, or sparse and shorter, respectively.

Semiquantitative method for counting fimbriae

We counted the number of fimbriae per cell from 203 and 74 photographs of 10–12 cells of parent and mutant strains, respectively, in which cells did not overlap. The fimbriae were counted near the cell surface, where they were not too bunched, under a magnifying glass (×8) on a negative film placed on a light box. Half of the fimbriae per cell were counted in this manner.

Hemagglutination activity

The hemagglutination titer of *P. gingivalis* was examined using the modified method of Chu *et al.* (13). Cell suspensions in liquid medium, taken from flasks prepared as described above, were diluted from eight- to 350-fold with saline and then mixed with an equal amount of 5% chicken erythrocytes in saline (Nippon Biotest, Tokyo, Japan) on blood test plates. To prevent damage of the fimbriae, the bacteria were not washed before the hemagglutination test, and mixed using a micropipette with a tip that had been cut with scissors. After 1 h of incubation at room temperature, the highest dilution of the bacterial cultures that induced hemagglutination was recorded.

To determine the optical density of the cells before dilution, cultures were thoroughly dispersed, liquid medium was replaced with saline by centrifugation, and the optical density of each cell suspension was measured by spectrophotometry at 600 nm (UV mini 1240; Shimadzu, Kyoto, Japan).

Preparation of SEM samples of *P. gingivalis* hemaggregates

Hemaggregates of *P. gingivalis* were collected from the bottom of blood test plates, placed on silane-coated glass slides using a micropipette and processed, as described above, for SEM.

Results

SEM observation of *P. gingivalis* aggregates of parent and mutant strains cultured in liquid medium

Cells of *P. gingivalis* with fimbriae were distinct (Fig. 1). Abundant cells of the parent strain adhered well to glass slides, whereas mutant cells adhered sparsely (Fig. 2). Aggregates of the parent strain were composed of long and abundant bacterial chains and clusters of 20–80 μm in diameter,

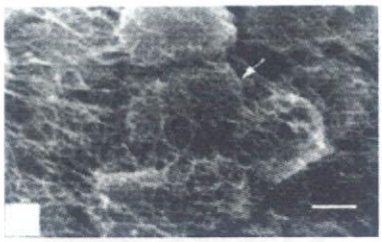

Fig. 1. Scanning electron micrograph of *Porphyromonas gingivalis* in parent strain cluster. Fimbriae bunch and form a dense meshwork containing embedded bacterial cells (arrow). Bar, 0.3 μm.

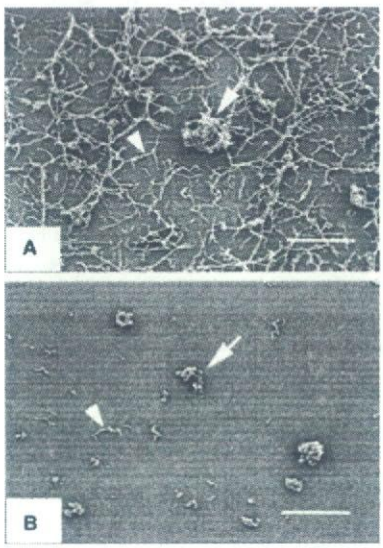

Fig. 2. Scanning electron micrograph of *Porphyromonas gingivalis* cultured in liquid medium. (A) Parent strain. (B) Mutant strain. Bar, 30 μm. More parent *P. gingivalis* strain is attached to slide than mutant. Chains of the parent strain are long and abundant, whereas chains of the mutant are short and sparse. Clusters and chains are indicated by arrows and arrowheads, respectively.

of which the margins were wreathed with chains (Figs 2A and 3A). In contrast, those of the mutant strain were composed of few chains and isolated clusters of 10–15 μm in diameter, but the margins were also wreathed with chains (Figs 2B and 3B). Aggregates of the mutant strain comprised shorter chains and smaller clusters than those of the parent strain.

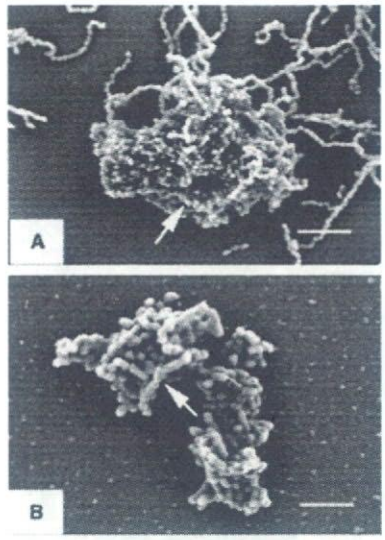

Fig. 3. Enlarged photographs of bacterial cluster shown in Fig. 1. (A) Parent strain. (B) Mutant strain. Bar, 3 μm. Clusters of parent and mutant strains are wreathed with chains (arrow).

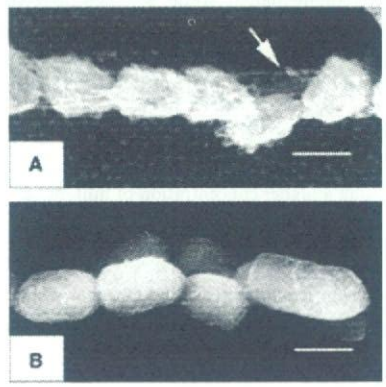

Fig. 4. Enlarged scanning electron micrograph of bacterial chains. (A) Parent strain. (B) Mutant strain. Bar, 0.5 μm. Fimbriae are rich on parent cells. Bacterial cells of parent strain in chains connect to other cells via dense meshworks (arrow) (A). In contrast, fimbriae are sparse in chains of the mutant strain and the fimbrial meshwork is virtually absent (B).

Cells of both strains were short rods of about 0.8 and 0.5 μm in long and short diameters, respectively. Cells of the parent strain had abundant fimbriae that formed dense fimbrial meshworks in bacterial chains and clusters (Figs 1, 4A and 5A). Cells in chains of the parent strain were connected to

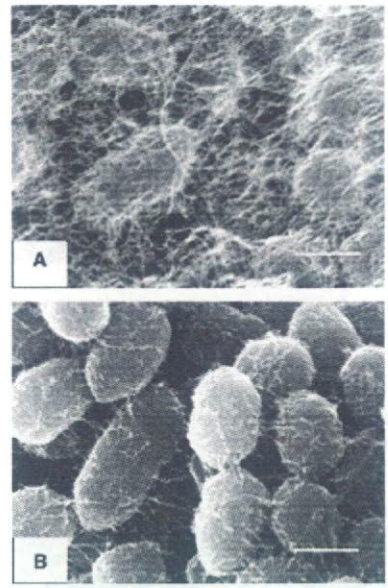

Fig. 5. Enlarged scanning electron micrograph of bacterial clusters. (A) Parent strain. (B) Mutant strain. Bar, 0.5 μm. Bacteria in parent strain clusters are connected by rich, long fimbriae that form dense meshworks (A); those of the mutant strain are connected by fewer, shorter fimbriae that form loose meshworks (B).

other cells by fimbria meshworks (Fig. 4A), whereas chains on the surface of mutant cells contained fewer and shorter fimbriae (Fig. 4B). Clusters of the parent strain contained bunched fimbriae that formed dense, large-scale meshworks with apparently embedded bacteria (Figs 1 and 5A). On the other hand, clusters of the mutant strain contained sparse fimbriae that formed loose meshworks in intercellular spaces (Fig. 5B).

Comparison of the number of fimbriae per cell in aggregates

The numbers of fimbriae per parent and mutant cell were 196.4 ± 23.6 and 93.2 ± 10.6 (means ± standard deviation), respectively. The parent strains contained about twice as many fimbriae as the mutant strain.

SEM observation of hemaggregates of parent and mutant cells

The dense fimbrial meshworks were detached from parent bacterial cells in

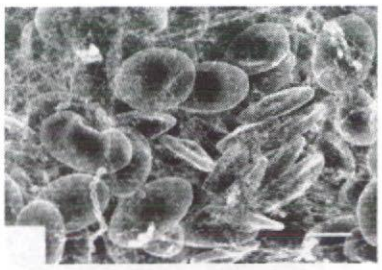

Fig. 6. Scanning electron micrograph of hemaggregate including *Porphyromonas gingivalis* of the parent strain. Erythrocyte aggregation by *P. gingivalis* of the parent strain is mediated by dense fimbrial meshwork including some bacterial cells. Bar, 10 μm.

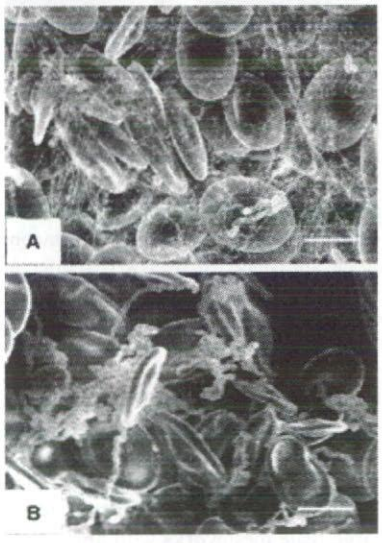

Fig. 7. Scanning electron micrograph of hemaggregates including *Porphyromonas gingivalis*. (A) Parent strain. (B) Mutant strain. Bar, 5 μm. Erythrocyte aggregation by the parent *P. gingivalis* strain is mediated by a dense fimbrial meshwork (A); that of the mutant strain appears to be mediated by bacterial clusters and chains (B). Hemagglutination was induced using a higher concentration of mutant cells than of parent cells.

hemaggregates and involved a few bacterial chains with aggregated erythrocytes (Figs 6, 7A and 8A). Bacterial chains with long fimbriae occasionally mediated hemagglutination (Fig. 9A). On the other hand, mutant bacterial chains and clusters appeared to mediate hemaggregation (Figs 7B and 8B). Mutant cells in

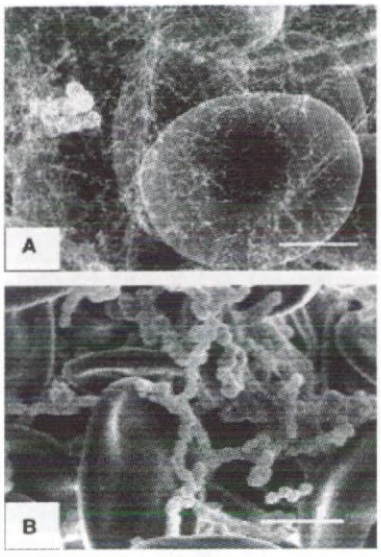

Fig. 8. Enlarged photographs of *Porphyromonas gingivalis* hemaggregate. (A) Parent strain. (B) Mutant strain. Bar, 3 μm. A dense fimbrial meshwork adheres to the surface of erythrocytes in the hemaggregates containing parent strain *P. gingivalis* (A). The meshwork consists of fimbriae detached from cells by using a micropipette to mix bacteria and erythrocytes. Bacterial chains and clusters adhere to the erythrocyte surface in hemaggregates of mutant *P. gingivalis* (B). Hemagglutination was induced using a higher concentration of mutant cells than of parent cells.

chains and clusters had shorter fimbriae than those of the parent strain in hemaggregates (Fig. 9B).

Comparison of hemagglutination titers

The minimal optical density of the parent and mutant strains required to induce hemagglutination, as calculated from the original optical density and the dilution factor, were 0.04 ± 0.02 and 0.4 ± 0.1 (means ± standard deviation) at 600 nm, respectively. Thus, the hemagglutination titer of the parent strain was 10-fold higher than that of the mutant strain.

Discussion

We obtained clear SEM images of *P. gingivalis* with fimbriae. The SEM images revealed that the powerful

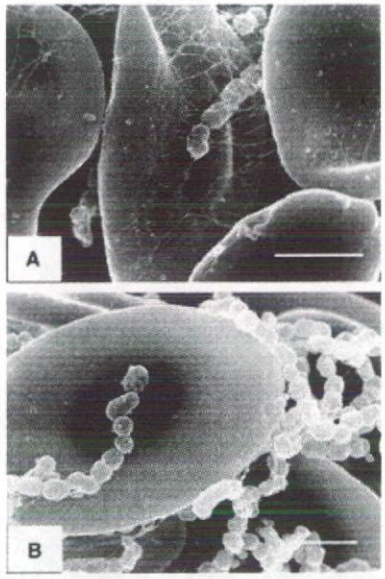

Fig. 9. Enlarged photographs of chains in aggregates of erythrocytes caused by *Porphyromonas gingivalis*. (A) Parent strain. (B) Mutant strain. Bar, 2 μm. Chains of bacterial cells with long fimbriae mediate hemagglutination in hemaggregates caused by the parent strain of *P. gingivalis* (A), and short fimbriae on mutant *P. gingivalis* cells, constituting chains or clusters, also mediate hemagglutination (B). Short fimbriae might be artifacts of mechanical disruption.

adhesiveness and hemagglutination activity depends on dense fimbrial meshworks and that the density of the meshwork depends on the number of fimbriae per cell. This study is the first to show morphological evidence of fimbrial adhesiveness and involvement in bacterial hemagglutination.

We observed fimbriae by SEM because we used a high-power SEM and an osmium plasma coater, incubated the cells in abundant medium and ensured minimal disruption of samples before fixation.

The hemagglutination titer of the parent strain was about 10-fold higher than that of the mutant strain. Optical density is a variable of a hemagglutination titer and reflects the numbers of cells and fimbriae in the sample. As the hemagglutination titer was not proportional to the number of fimbriae per cell, the high hemagglutination titers of the parent strain can be explained by the presence of the dense fimbrial meshwork.

Mutant cells contained fewer and shorter fimbriae in aggregates than the parent strain. We consider that aggregation is difficult because the fimbriae were sparse, and thus easily damaged during sample preparation. The mutant fimbriae in aggregates differed from those, ≈ 0.1 μm in length, described by Park *et al.* (14).

Slots & Gibbons (15) and Okuda *et al.* (16) have shown physiological evidence that fimbriae have adhesive properties and that isolated fimbriae can induce hemagglutination. The former observed fimbrial aggregates in hemaggregates by transmission electron microscopy. Our SEM study revealed a detached dense fimbrial meshwork that mediated hemagglutination. We used a pipette to mix the bacterial cells and erythrocytes on blood test plates. Thus, fimbriae detached from the cells by mechanical disruption formed a dense meshwork that mediated hemagglutination. This finding indicates that the fimbriae themselves are adhesive.

Noiri *et al.* (6) immunohistochemically localized *P. gingivalis* fimbriae in periodontal biopsy tissues obtained from patients with severe periodontitis. They found that *P. gingivalis* fimbriae localize in plaques attached to the cementum. The dense fimbrial meshwork of *P. gingivalis* observed in the present study probably contributes to the attachment of plaques to the cementum, which is the optimal location for alveolar bone resorption.

The SEM images of aggregates of *P. gingivalis* of the parent strain suggest how fimbriae support the process of colonization. Two daughter cells of *P. gingivalis* were connected with fimbriae along the long axis of rods. Thus, the repetition of amitosis causes the formation of long chains supported by fimbrial meshwork.

A bacterial cluster might then be formed by chain aggregation, because the surfaces of clusters were wreathed with such chains. When chains become dense, each cell in a chain connects to other cells in neighboring chains via fimbriae, forming fimbrial meshworks.

Subgingival plaque contains live and dead bacteria (17) and endotoxin released from dead *P. gingivalis* stimulates bone resorption (18). When released deep inside large plaques, endotoxin might diffuse smoothly through fimbrial meshworks.

In conclusion, the presence of rich fimbriae helps *P. gingivalis* to form dense fimbrial meshworks that prominently enhance its adhesiveness. Thus, *P. gingivalis* forms plaques with other bacteria in deep subgingival pockets and becomes a potential threat within the oral cavity.

References

1. Ximenez-Fyvie LA, Haffajee AD, Socransky SS. Microbial composition of supra and subgingival plaque in subjects with adult periodontitis. *J Clin Periodontol* 2000;**27:**722–732.
2. Iino Y, Hopps RM. The bone resorbing activities in tissue culture of lipopolysaccharides from the bacteria *Actinobacillus actinomycetemcomitans*, *Bacteriodes gingivalis* and *Capnocytophaga ochracea* isolated from human mouths. *Arch Oral Biol* 1984;**29:**59–63.
3. Hamada S, Koga T, Nishihara T, Fujiwara T, Okahashi N. Characterization and immunobiologic activities of lipopolysaccharides from periodontal bacteria. *Adv Dent Res* 1988;**2:**284–291.
4. Takazoe I, Nakamura T, Okuda K. Colonization of the subgingival area by *Bacteroides gingivalis*. *J Dent Res* 1984;**63:**422–426.
5. Yoshimura A, Hara Y, Kaneko T, Kato I. Secretion of IL-1α, TNF-α, IL-8 and IL-1ra by human polymorphonuclear leukocytes in response to lipopolysaccharides from periodontopathic bacteria. *J Periodont Res* 1997;**32:**279–286.
6. Noiri Y, Li L, Yoshimura F, Ebisu S. Localization of *Porphyromonas gingivalis*-carrying fimbriae *in situ* in human periodontal pockets. *J Dent Res* 2004;**12:** 941–945.
7. Cutler CW, Kalmar JR, Genco CA. Pathogenic strategies of the oral anaerobe, *Porphyromonas gingivalis*. *Trends Microbiol* 1995;**3:**45–51.
8. Watanabe K, Yamaji Y, Umemoto T. Correlation between cell-adherent activity and surface structure in *Porphyromonas gingivalis*. *Oral Microbiol Immunol* 1992;**7:**357–363.
9. Du L, Pellen-Mussi P, Chandad F, Mouton C, Bonnaure-Mallet M. Fimbriae and the hemagglutinating adhesin, HA-Ag2 mediate adhesion of *Porphyromonas gingivalis* to epithelial cells. *Infect Immun* 1997;**65:**3875–3881.
10. Onoe T. Detection and characterization of gene products related to fimbriae from. *Porphyromonas gingivalis Aichi-Gakuin J Dent Sci* 1997;**35:**207–216 [in Japanese with English abstract].
11. Hongo H, Osano E, Ozeki M *et al.* Characterization of an outer membrane protein gene, PgmA, and its gene product from *Porphyromonas gingivalis*. *Microbiol Immunol* 1999;**43:**937–946.
12. Fletcher HM, Schenkein HA, Morgan RM, Bailey K, Berry CR, Macrina FL. Virulence of a *Porphyromonas gingivalis* W83 mutant defective in the *prtH* gene. *Infect Immun* 1995;**63:**1521–1528.
13. Chu L, Bramanti TE, Ebersole JL, Holt SC. Hemolytic activity in the periodontal pathogen *Porphyromonas gingivalis*: kinetics of enzyme release and localization. *Infect Immun* 1991;**59:**1932–1940.
14. Park Y, Simionato R, Sekiya K *et al.* Short fimbriae of *Porphyromonas gingivalis* and their role in coadhesion with *Streptococcus gordonii*. *Infect Immun* 2005;**73:**3983–3989.
15. Slots J, Gibbons RJ. Attachment of *Bacteroides melaninogenicus* subsp. *asaccharolyticus* to oral surfaces and its possible role in colonization of the mouth and of periodontal pockets. *Infect Immun* 1978;**19:**254–264.
16. Okuda K, Slots J, Genco RJ. *Bacteroides gingivalis*, *Bacteroides asaccharolyticus*, and *Bacteroides melaninogenicus* subspecies: cell surface morphology and adherence to erythrocytes and human buccal epithelial cells. *Current Microbiol* 1981;**6:**7–12.
17. Hope CK, Clements D, Wilson M. Determining the spatial distribution of viable and nonviable bacteria in hydrated microcosm dental plaques by viability profiling. *J Appl Microbiol* 2002;**93:**448–455.
18. Ito HO, Shuto T, Takeda H *et al.* Lipopolysaccharides from *Porphyromonas gingivalis*, *Prevotella intermedia* and *Actinobacillus actinomycetemcomitans* promote osteoclastic differentiation *in vitro*. *Arch Oral Biol* 1996;**41:**439–444.

Available online at www.sciencedirect.com
ScienceDirect
Talanta 74 (2008) 1265–1270
Talanta
www.elsevier.com/locate/talanta

Affinity-based elimination of aromatic VOCs by highly crystalline multi-walled carbon nanotubes

Hiroaki Sone [a], Bunshi Fugetsu [a,*], Takayuki Tsukada [b], Morinobu Endo [c,*]

[a] *Graduate School of Environmental Science, Hokkaido University, Sapporo 060-0810, Japan*
[b] *Nano Carbon Technologies Co. Ltd., 600 Tanaka-cho, Akishima, Tokyo, Japan*
[c] *Faculty of Engineering, Shinshu University, 4-17-1 Wakasato, Nagano-shi 380-8553, Japan*

Received 6 August 2007; received in revised form 29 August 2007; accepted 29 August 2007
Available online 7 September 2007

Abstract

Carbon nanotubes (CNTs) are capable of adsorbing pollutant chemicals. Their adsorptive capacities and adsorbing mechanisms, however, are not fully understood. As-grown CNTs often contain both crystalline and amorphous carbon, and the ratio of carbon types can affect adsorption. In this study, highly crystalline multi-walled carbon nanotubes (HC-MWCNTs) were used as the adsorbent for volatile organic compounds (VOCs) in contaminated air samples. Air containing 23 added VOCs (1,1-dichloroethylene, dichloromethane, *trans*-1,2-dichloroethylene, *cis*-1,2-dichloroethylene, chloroform, 1,1,1-trichloroethane, carbon tetrachloride, 1,2-dichloroethane, benzene, trichloroethylene, 1,2-dichloropropane, bromodichloromethane, *cis*-1,3-dichloropropene, toluene, *trans*-1,3-dichloropropene, 1,1,2-trichloroethane, tetrachloroethylene, dibromochloromethane, *m*-xylene, *p*-xylene, *o*-xylene, bromoform, and *p*-dichlorobenzene) was used for model samples. Adsorptive experiments were carried out by passing the air samples through a cartridge packed with HC-MWCNTs. Initial results showing high selectivity and high affinity for adsorbing aromatic VOCs (benzene, toluene, *m*-xylene, *p*-xylene, *o*-xylene, and *p*-dichlorobenzene) have provided new insight into the adsorption mechanisms. Data suggest that the HC-MWCNTs, unlike conventional carbon materials, adsorb aromatic compounds according to Fukui's frontier theory, which is based on the interactions between the HOMO and LUMO of the aromatic VOCs and those of the HC-MWCNTs.
© 2007 Elsevier B.V. All rights reserved.

Keywords: Highly crystalline multi-walled carbon nanotubes (HC-MWCNTs); Volatile organic compounds (VOCs); Affinity-based adsorption; LUMO–HOMO interaction

1. Introduction

Volatile organic compounds (VOCs) have received a great deal of attention in the field of environmental control for a number of reasons. First, VOCs are ubiquitous in the environment, workplace, and consumer products [1–4]. Humans can, therefore, be easily exposed to VOCs through skin contact, breathing, and eating. Second, VOCs are suspected to have primary and secondary harmful effects [5,6] due to prolonged exposure. These include eye and throat irritation, liver damage, and damage to the central nervous system. Third, VOCs can form photochemical smog, which contains ozone and other toxic byproducts, by reacting with other atmospheric chemicals such as nitrogen oxides [7]. Moreover, VOCs are emitted by landfill leachate and industrial effluent. Leakage into groundwater can cause serious contamination problems [8].

Among VOCs, the aromatic compounds, especially benzene, toluene, xylene and dichlorobenzene, are of particular interest. All of the aromatic VOCs are known or suspected to be carcinogenetic [9]. Furthermore, these compounds have no safety threshold dose for carcinogenic effects. Thus, even low-level exposure poses a finite risk. In fact, benzene, toluene, and xylenes, known as BTX, are the markers for human exposure to VOCs [10].

In the not-so-distant past, adsorptive treatment using activated carbon as the adsorbent was deployed for VOCs elimination [11–13]. However, the inability of activated carbon to selectively adsorb aromatic compounds results in an unpredictable lifespan for the carbon; the selectivity problem needs

* Corresponding authors.
E-mail addresses: hu@ees.hokudai.ac.jp (B. Fugetsu), endo@endomoribu.shinshu-u.ac.jp (M. Endo).

0039-9140/$ – see front matter © 2007 Elsevier B.V. All rights reserved.
doi:10.1016/j.talanta.2007.08.041

to be addressed. Over the last decade, growing effort has been devoted to developing and utilizing new carbon materials for VOCs elimination. The so-called carbon nanotubes (CNTs) are especially promising because of their unique properties. CNTs can be divided into multi-walled carbon nanotubes (MWCNTs) and single-walled carbon nanotubes (SWCNTs) based on the carbon atom layers in the walls of the tubes. MWCNTs have been known for more than 30 years [14] and SWCNTs for 14 years [15,16]. The hexagonal arrays of sp^2-like carbon atoms in the tubular graphene sheets on the surfaces of CNTs provide a favorable morphological structure for adsorbing aromatic compounds. Long and Yang [17] have used MWCNTs as an adsorbent for the removal of dioxin from model air samples. They found the adsorptive capability of CNTs to be much higher than that of conventional activated carbon, especially in the Henry's law region. Li et al. [18] employed MWCNTs as an adsorbent for solid-phase extraction of VOCs from model water samples. The MWCNTs exhibited excellent extraction capability and high recoverability [18,19]. These studies have provided experimental evidence that CNTs are capable of adsorbing pollutants. Nevertheless, none of these studies has explored the possibility of using CNTs as an adsorbent for separating aromatic VOCs from other types of VOCs.

This study presents the first data on the use of CNTs as an adsorbent for selectively eliminating aromatic VOCs. Model air samples containing six aromatic VOCs and 17 aliphatic VOCs were passed through a CNT-packed cartridge, and the amount of VOCs retained by the CNTs was quantitatively analyzed using GC–MS. The CNTs were found to be capable of selectively adsorbing the aromatic VOCs. This is also the first study to describe the possible mechanism for the adsorption of aromatic compounds by CNTs using an orbital framework (Fukui's frontier orbital theory).

2. Materials and methods

2.1. Preparation of the model air samples containing VOCs

A commercially available methanol solution (Wako Pure Chemicals) containing six aromatic VOCs (benzene, toluene, *m*-, *p*-, *o*-xylene, and *p*-dichlorobenzene) and 17 aliphatic VOCs (1,1-dichloroethylene, dichloromethane, *trans*-1,2-dichloroethylene, *cis*-1,2-dichloroethylene, chloroform, 1,1,1-trichloroethane, carbon tetrachloride, 1,2-dichloroethane, trichloroethylene, 1,2-dichloropropane, bromodichloromethane, *cis*-1,3-dichloropropene, *trans*-1,3-dichloropropene, 1,1,2-trichloroethane, tetrachloroethylene, dibromochloromethane and bromoform) was used for preparing the model air samples. Most compounds were present at a concentration of 1.0 mg/mL, except for *m*-xylene and *p*-xylene (*m*-xylene + *p*-xylene = 1.0 mg/mL). The model air samples were generated by using a syringe to inject 100 μL of the VOCs mixture into a 10-L tetra-bag that was previously filled with purified air under ambient pressure. The injection valve was immediately switched to the closed position and the tetra-bag was then heated at 80 °C in an oven for 1 h. Samples prepared in this manner were used for the adsorptive studies.

2.2. Highly crystallized multi-walled carbon nanotubes (HC-MWCNTs)

Highly crystalline multi-walled carbon nanotubes (HC-MWCNTs) were used as the adsorbent throughout this study. The HC-MWCNTs were produced using the floating reactant method [20–22]. Ferrocene was used as the catalyst precursor and toluene was used as the carbon feedstock, with hydrogen as the carrier gas. A toluene solution containing a specified amount of ferrocene was fed into a reactor with a temperature of approximately 1200 °C to produce the "as-grown" nanotubes. These nanotubes contain a substantial portion of amorphous carbon. The resultant nanotubes were further thermally annealed at 2600 °C for 30 min in a highly purified argon gas atmosphere to produce the HC-MWCNTs. MWCNTs and SWCNTs containing relatively large amounts of amorphous carbon were also prepared in the laboratory using the CVD method, and these "as-grown" CNTs were used as comparison adsorbents.

2.3. Laboratory-made CNT-packed cartridges

CNT-packed cartridges were made by dispersing carbon nanotubes in methanol using an ultrasonic generator (42 kHz) and then loading the CNTs into an empty cartridge (tubular shaped polypropylene: length, 16.5 mm; internal diameter, 10 mm) using a vacuum pump. The final mass of CNTs in each cartridge was approximately 80 mg. Polypropylene filters (10 μm) were placed at each end of the cartridges to hold the CNTs in place.

2.4. Adsorption and desorption of VOCs

The inlet end of the CNT-packed cartridge was connected to the sample bag. The other end was connected to a Sibata charcoal tube (Sibata, Tokyo, Japan), which is a glass tube filled with activated carbon and is used as the domestic standard cartridge for sampling VOCs in indoor air samples. In these experiments, the charcoal tube was used to trap any VOCs not retained by the CNT-packed cartridge. The outlet end of the tube was connected to a vacuum pump and the air samples were passed through the cartridges at an adjustable flow rate.

To measure the amounts of VOCs trapped by the charcoal, the tube was extracted with 5.0 mL CS_2. Analysis was performed with a Shimadzu GCMS-QP5050A system, using toluene D8 as the internal standard. The VOCs adsorbed by the CNT cartridge were estimated by subtraction of the VOCs retained by the charcoal from the initial quantities injected into the sample bag. Adsorptive and desorptive experiments were conducted in triplicate for each sample.

3. Results and discussion

3.1. Characteristics of the highly crystalline multi-walled carbon nanotubes (HC-MWNTs)

Fig. 1 shows typical SEM images of the HC-MWCNTs at low (upper photo) and high (lower photo) resolutions. Tubes with

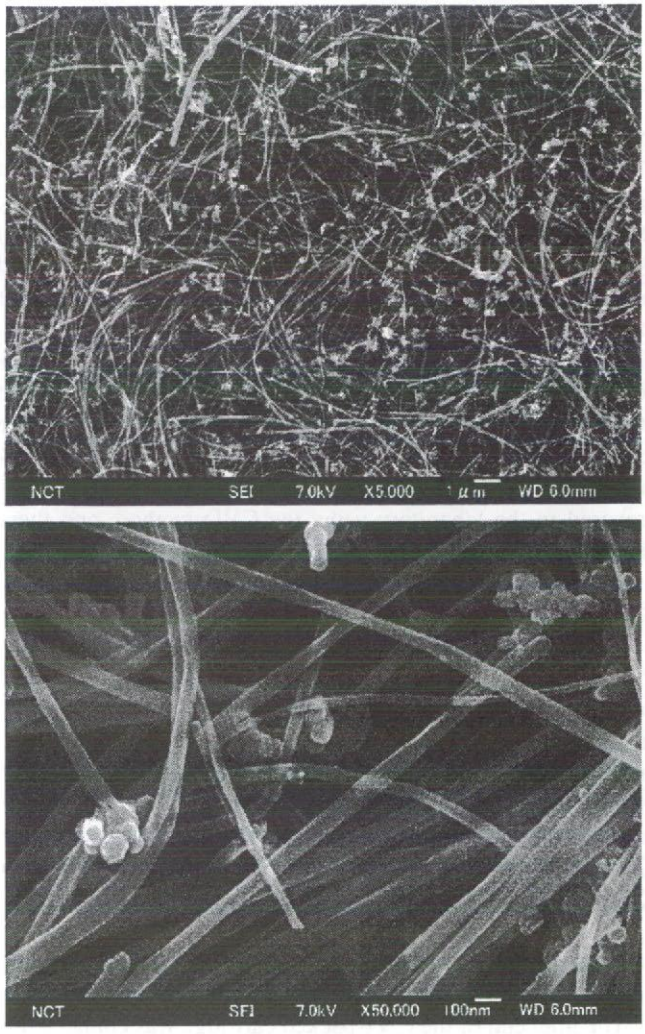

Fig. 1. SEM images of the HC-MWCNTs at low (upper photo) and high (lower photo) resolutions.

external diameters ranging from 40 to 90 nm were observed, together with a few carbon nano-particles. According to X-ray elemental analysis, the metallic impurity of the HC-MWCNTs was less than 450 ppm. The specific surface area (measured by N_2 adsorption based on the BET method) was 25 m^2/g.

Analysis using Raman spectroscopy (Fig. 2) revealed an extremely small *R*-value, which is the ratio of the intensity of the D band (1350 cm^{-1}) to that of the G band (1582 cm^{-1}). This indicates that the thermally annealed tubes were highly crystalline. Also, the G′ band, which corresponds to the overtone of 2D at 2700 cm^{-1}, was very intensive and symmetric for the HC-MWCNTs.

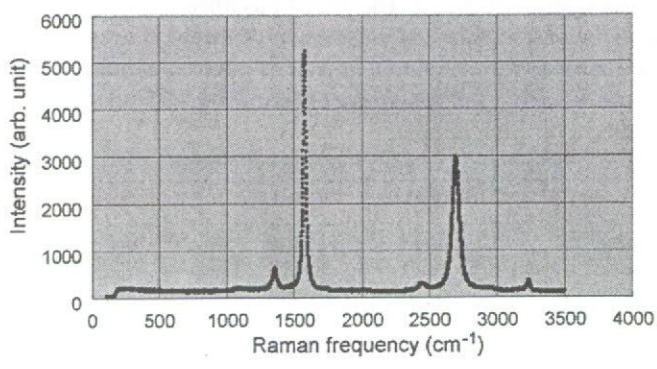

Fig. 2. Raman spectroscopy for the HC-MWCNTs.

Table 1
GC–MS conditions for quantitative VOCs determination

Chromatograph	
Column	DB-624, length: 60 m, ϕ: 0.25 mm, Film: 1.4 μm
Carrier gas	He
Total flow	50 mL/min
Split ratio	24
Injector temperature	200 °C
Detector temperature	230 °C
Oven temperature program	50 °C (2 min) to (10 °C/min) to 100 °C (5 °C/min) to 130 °C (10 °C/min) to 190 °C (5 min)
Mass spectrometer	
Interface temperature	230 °C
Electron multiplier voltage	1.0 kV
Scan mode	SIM

3.2. Adsorptive studies

In early experiments, only HC-MWCNT-packed cartridges were used as the adsorptive medium. However, difficulties were encountered in extracting VOCs from the cartridge. A small amount of the carbon nanotubes became entrained in the extraction solution and needed to be removed before the samples could be injected into the GC–MS system. Some of the extracted VOCs were lost during this extra step and recoveries were unsatisfactory. This difficulty was overcome by connecting a standard Sibata charcoal tube next to the HC-MWCNT-packed cartridge. The VOCs retained by the charcoal tube were extracted using CS_2 and the extraction solution was directly analyzed using GC–MS. Operating conditions for the GC–MS are summarized in Table 1.

Table 2 shows recoveries for four groups of standard samples processed using only the charcoal tube (no HC-MWCNT-packed cartridge). The samples were heated in an oven for 1 h at 50, 60, 70, and 80 °C, respectively. Recoveries were slightly dependent on the temperature (Table 2) and the best recoveries (from 93.9% to 106.3%) were obtained at 80 °C. Note that *m*-xylene and *p*-xylene were unable to be measured separately using this GC–MS system.

3.3. Affinity of HC-MWCNTs for aromatic VOCs

Average values for adsorption (μg VOCs/g HC-MWCNTs) are shown in Fig. 3. The HC-MWCNTs-packed cartridges demonstrated a high capacity for adsorbing *p*-dichlorobenzene, *o*-xylene, *m*-, *p*-xylene, toluene, and benzene (i.e., the aromatic VOCs). The adsorption capacity of the HC-MWCNTs for adsorbing *p*-dichlorobenzene was 1048.3 μg/g. For *o*-xylene, *m*,*p*-xylene, toluene, and benzene, adsorption capacities were